Journal of Materials Chemistry B

PAPER

View Article Online
View Journal | View Issue

Cite this: J. Mater. Chem. B, 2016, 4, 3721

Formation of $CaCO_3$ fibres directed by polypeptide vesicles†

Yingqing Lu, Chunhua Cai,* Jiaping Lin* and Qixin Zhuang

Received 25th March 2016,
Accepted 19th April 2016

DOI: 10.1039/c6tb00759g

www.rsc.org/MaterialsB

Mineralization behaviour of $CaCO_3$ in the presence of polypeptide vesicles self-assembled from poly(L-glutamic acid)-*block*-poly(propylene oxide)-*block*-poly(L-glutamic acid) (PLGA-*b*-PPO-*b*-PLGA) triblock copolymers was studied. Under the mediation of PLGA-*b*-PPO-*b*-PLGA vesicles, $CaCO_3$ fibre clusters were obtained. The structure of fibres could be regulated by the mineralization temperature, copolymer composition, copolymer concentration, and Ca^{2+} concentration. The investigation of the fibre growth process suggested a solution–precursor–solid mechanism *via* transient amorphous precursors. Since the polypeptide vesicles could serve as both the modifier and template for the formation of amorphous precursors, the properties of amorphous precursors were affected by the vesicular structure. The variation in the fibre structure was ascribed to the different aggregation and transformation behaviours of amorphous particles. These findings can provide useful information for the design of novel inorganic materials with fibrous structures and enrich our existing knowledge of the crystallization process from the amorphous phase.

Introduction

Biominerals, acting as an essential part in living organisms, are well known for their hierarchical organization, complex shape, controlled polymorphs, and superior material properties.[1,2] Because of their fascinating characteristics and theoretical and practical values, biominerals have attracted widespread interest.[3–6] It has been demonstrated that the formation of biominerals in organisms can be regulated by mineral proteins.[7–9] During the biomineralization process, the hydrophilic peptide residues of the proteins can interact with minerals and the hydrophobic residues offer scaffolds for heterogeneous nucleation.[10–12] Inspired by protein-controlled biomineralization, synthetic polypeptides such as poly(L-glutamic acid) (PLGA), poly(aspartic acid) (PAsp), poly(L-lysine) (PLL), and their derivates have been used as additives for mineralization.[13,14] For example, Gower *et al.* found that under the mediation of hydrophilic polyanionic polypeptides (containing aspartic acid and phosphoserine), smooth $CaCO_3$ films were produced *via* a polymer-induced liquid-precursor process.[15] Meldrum *et al.* used PAsp to synthesize amorphous calcium carbonate with different short-range structures.[16] However, the hydrophilic polypeptides are structurally different from mineral proteins because proteins are generally amphiphilic and folded into defined nanostructures.[17–19]

As revealed by recent achievements in supramolecular chemistry, amphiphilic copolymers comprising hydrophilic polypeptide segments can self-assemble into aggregates with diverse structures.[20–22] These aggregates could mimic the role of proteins in mineralization, because the polypeptide segments in the aggregates can interact with minerals and the self-assembled structures can act as mineralization templates. These features make polypeptide aggregates suitable additives for biomimetic mineralization.[23–25] For instance, spherical $CaCO_3$ crystals with porous structures were prepared using poly(ethylene glycol)-*block*-poly(aspartic acid) (PEG-*b*-PAsp) micelles.[26] Our group used polypeptide micelles to regulate the structures of $CaCO_3$ and $BaCO_3$ minerals.[27,28] For example, we found that poly(*N*-isopropyl acrylamide)-*block*-PLGA micelles can induce the formation of $BaCO_3$ crystals with a spiral belt morphology, which is similar to the spiral morphology of aragonite on the inner surface of nacre.[28] However, so far the studies regarding polypeptide aggregate mediated mineralization are still limited. Especially, the mineralization regulated by polypeptide aggregates other than micelles, such as vesicles, has barely been considered.

In biomineralization, vesicles are found to serve as reaction compartments or transporters.[29–32] Vesicles can adjust the ratio of ionic species and supply a confined aqueous environment for crystal growth. For example, in the formation of coccolith exoskeletons, the growth of $CaCO_3$ crystals occurs in cytoskeletal

Shanghai Key Laboratory of Advanced Polymeric Materials, State Key Laboratory of Bioreactor Engineering, Key Laboratory for Ultrafine Materials of Ministry of Education, School of Materials Science and Engineering, East China University of Science and Technology, Shanghai 200237, China. E-mail: jlin@ecust.edu.cn, caichunhua@ecust.edu.cn; Tel: +86-21-64253370

† Electronic supplementary information (ESI) available: ^{1}H NMR spectra of PBLG-*b*-PPO-*b*-PBLG and PLGA-*b*-PPO-*b*-PLGA copolymers, GPC traces of PBLG-*b*-PPO-*b*-PBLG copolymers, SEM images and FTIR spectra of $CaCO_3$ samples mediated by PPO or PLGA homopolymers. See DOI: 10.1039/c6tb00759g

vesicles and the bulk coccolith shape is determined by the vesicle shape.[31] The mineralization of magnetite in magnetotactic bacteria was also found to proceed in vesicles, where the orientation and length of magnetite chains can be precisely controlled by transmembrane proteins.[29] These examples demonstrate the potential of vesicles in regulating the mineralization process. More attention should be devoted to vesicle-induced biomimetic mineralization.

Among the multifarious micromorphologies of biominerals, the fibrous morphology has received much attention owing to its prevalence in the teeth of both vertebrates and invertebrates.[33,34] For instance, the keel and stone regions of sea-urchin teeth consist of highly regulated calcite fibres, which are embedded in an amorphous matrix.[35] Therefore, it is expected that the fibre formation strategy can be applied to produce inorganic materials with regulated crystallographic properties. Several hypotheses have been proposed on the mechanism of fibre formation, such as oriented attachment,[36] directional aggregation processes,[37,38] and solution–precursor–solid (SPS) processes.[39,40] Nonetheless, it is still a challenge to control the structure of fibrous minerals.

In this work, vesicles self-assembled from poly(L-glutamic acid)-*block*-poly(propylene oxide)-*block*-poly(L-glutamic acid) (PLGA-*b*-PPO-*b*-PLGA) triblock copolymers were used to mediate $CaCO_3$ mineralization. In the presence of PLGA-*b*-PPO-*b*-PLGA vesicles, $CaCO_3$ fibres were obtained. The structure of fibres could be regulated by mineralization temperature, copolymer composition, copolymer concentration, and Ca^{2+} concentration. The investigation of the mineralization process revealed that the fibres were formed through the SPS process *via* a transient amorphous phase. The variation in the fibre structure was ascribed to the different aggregation and transformation behaviours of amorphous precursors. These findings can not only help us for a better understanding of the formation and transformation of the amorphous phase in biomineralization, but also offer useful information for designing inorganic materials with a controllable fibrous structure.

Experiment

Materials and reagents

α,ω-Amino poly(propylene oxide) (NH_2-PPO-NH_2, M_n = 4000, Sigma Aldrich) was dialyzed against water to remove impurities and lyophilized. γ-Benzyl-L-glutamate-*N*-carboxyanhydride (BLG-NCA) was synthesized according to the procedures reported in the literature.[41–44] Deionised water (DIW) was prepared in a Millipore Super-Q Plus Water System to a level of 18.2 MΩ cm resistance. 1,4-Dioxane was refluxed with sodium and distilled immediately before use. $(NH_4)_2CO_3$, $CaCl_2$, and other chemicals were purchased from Adamas-beta and used as received. The glassware for crystallization was sonicated in ethanol for 10 min. It was then soaked in a H_2SO_4 (98 wt%)–H_2O_2 (7 : 3 v/v) solution, and rinsed with DIW. Afterward, it was rinsed with acetone and dried in air.

Synthesis of PLGA-*b*-PPO-*b*-PLGA triblock copolymers

Poly(γ-benzyl-L-glutamate)-*block*-poly(propylene oxide)-*block*-poly(γ-benzyl-L-glutamate) (PBLG-*b*-PPO-*b*-PBLG) triblock copolymers were first synthesized by the ring-opening polymerization of BLG-NCA initiated by NH_2-PPO-NH_2 in anhydrous 1,4-dioxane. PLGA-*b*-PPO-*b*-PLGA copolymers were then prepared by the hydrolyzation of PBLG blocks with potassium hydroxide (KOH). The details of the synthesis procedure can be found in our previous work.[22,45]

The composition of PBLG-*b*-PPO-*b*-PBLG copolymers was determined by ^{1}H NMR spectra. A typical ^{1}H NMR spectrum of PBLG-*b*-PPO-*b*-PBLG copolymers is given in Fig. S1a (ESI†). Since the degree of polymerization (DP) of the PPO block was known, the total molecular weights of the triblock copolymers could be calculated by the peak intensities of the methylene proton signal (5.1 ppm) of the polypeptide and the methylene proton signal (3.6 ppm) of PPO in the ^{1}H NMR spectrum. The deprotection of the benzyl group after hydrolyzation was confirmed by the disappearance of the methylene proton peak (5.1 ppm) in the ^{1}H NMR spectrum of PLGA-*b*-PPO-*b*-PLGA copolymers (Fig. S1b, ESI†). The molecular weight distributions of PBLG-*b*-PPO-*b*-PBLG triblock copolymers were determined by gel permeation chromatography (GPC) using DMF/LiBr as an eluent. GPC traces of the PBLG-*b*-PPO-*b*-PBLG block copolymers with various PBLG lengths are presented in Fig. S2 (ESI†). Three copolymers denoted by GPG36, GPG61, and GPG124 were prepared in our work. The numbers ''36'', ''61'', and ''124'' denote the PLGA repeating units on each side of the chain. Detailed information regarding the characteristics of triblock copolymers is shown in Table 1.

Preparation of polypeptide vesicles

The PLGA-*b*-PPO-*b*-PLGA copolymers were first dissolved in aqueous solution at 5 °C. Then the vesicles were prepared by raising the temperature of the solution. In a typical experiment, 20 mg PLGA-*b*-PPO-*b*-PLGA was dissolved in 10 mL NaOH solution. Then 33 mg (0.3 mmol) $CaCl_2$ was added as the calcium source of $CaCO_3$. The pH value of the solution was carefully adjusted to around 5.0 by HCl, NaOH, and DIW. The volume of the final solution was fixed at 20 mL. The solution was filtered through a 0.45 μm millipore filter (made from mixed cellulose esters) to remove impurities. All these procedures were conducted at 5 °C, where the PPO blocks could be dissolved well. Finally, the solution was put in a 20, 35, or 50 °C constant temperature oven for at least 4 h. At these temperatures, the PPO blocks became insoluble and the

Table 1 Characteristics of PLGA-*b*-PPO-*b*-PLGA copolymers

Sample	Copolymer[a]	M_n[b] (kg mol^{-1})	M_w/M_n[c]
GPG36	$PLGA_{36}$-*b*-PPO_{68}-*b*-$PLGA_{36}$	13.3	1.24
GPG61	$PLGA_{61}$-*b*-PPO_{68}-*b*-$PLGA_{61}$	19.7	1.25
GPG124	$PLGA_{124}$-*b*-PPO_{68}-*b*-$PLGA_{124}$	36.0	1.31

[a] The composition of the copolymers was derived from the ^{1}H NMR spectrum of the precursor PBLG-*b*-PPO-*b*-PBLG in $CDCl_3$ and TFA-d mixture solution. [b] The number-average molecular weights M_n of the PLGA-*b*-PPO-*b*-PLGA were calculated from the composition given in the second column. [c] The molecular weight distribution, M_w/M_n (M_w is the weight-average molecular weight), of the precursor PBLG-*b*-PPO-*b*-PBLG was determined by GPC.

copolymers self-assembled into vesicles.[46] The solutions of vesicles with various polymer concentrations were prepared by changing the initial polymer concentration at 5 °C.

Mineralization of $CaCO_3$

Mineralization was performed by gently pipetting the $(NH_4)_2CO_3$ solution into polypeptide vesicle solution containing $CaCl_2$.[47] In a typical experiment, 5 mL of the polymer solution and some glass wafers were put in a 10 mL bottle. The bottle was covered and placed in a constant temperature oven for more than 4 h. Then $(NH_4)_2CO_3$ (0.1 mol L^{-1}) solution was slowly pipetted into the solution. The final ratio of Ca^{2+} and CO_3^{2-} was 1 : 1. The precipitate was allowed to deposit for 48 h and then the wafers were taken out for further characterization after rinsing with DIW and drying in air.

In order to analyze the composition and structure of intermediates, we collected the precursors formed after 30 min mineralization by centrifuging 150 mL of the reaction solution at 6500 rpm for 5 min. The precipitates formed after 60 min mineralization were collected by scraping the precipitates from the bottom of the glass bottles. The collected samples were lyophilized before analysis.

Measurements

Scanning electron microscopy (SEM). The morphologies of minerals were observed by SEM (JSM-6460, JEOL) at an accelerating voltage of 10 kV. Samples were deposited on glass wafers and sputtered with gold before observations.

High-resolution transmission electron microscopy (HR-TEM) and selective area electronic diffraction (SAED). The HR-TEM and SAED were performed on a JEM-2100F HR-TEM operated at an acceleration voltage of 200 kV. The precipitate was scraped from the glass wafer and dispersed in water. Then, the sample was transferred to a copper grid with a carbon film and dried in air or in a vacuum. The sample of precursors was formed within 30 min mineralization, which was prepared by placing a drop of reaction solution on a film-coated copper grid, and then drying the solution in a vacuum.

Turbidity measurements (OD). The optical density (turbidity) of the copolymer solution was measured at a wavelength of 500 nm using a quartz cell (path length: 1 cm) with a UV-Vis spectrophotometer (UV-Vis UV-2550 SHIMADZU).

Electrophoresis measurements. The zeta potentials (ξ) of vesicles were measured using a Malvern Zetaseizer 3000HS. Each sample was measured three times.

X-ray diffraction (XRD). XRD patterns were recorded on Rigaku D/Max-2550V with Cu-Kα radiation in the range 2θ = 10–80°. The samples were scraped from the glass wafers and ground to form powders with a small particle size.

Fourier transform infrared spectroscopy (FT-IR). For FT-IR analysis, the samples were pressed with KBr into pellets. The spectra of the samples were recorded on a Nicolet 5700 FT-IR spectrometer in transmission mode.

Laser light scattering measurements. Light scattering measurements were performed using an ALV laser goniometer, with a 22 mW linearly polarized He-Ne laser (λ = 632.8 nm) and an ALV-5022 multiple tau digital correlator. All samples were diluted to 0.1 g L^{-1} and filtered through 0.8 μm filters to remove dust at 20, 35 or 50 °C before the light scattering measurements.

Dynamic light scattering (DLS) was used to obtain the hydrodynamic radius ($\langle R_h \rangle$) of GPG vesicles and detect the changes in the apparent size of the aggregates in the early stage of mineralization. The Laplace inversion of each measured intensity–intensity time correlation function $G^{(2)}(t,q)$ in the self-beating mode can result in a line width distribution $G(\Gamma)$. The translational diffusion coefficient D calculated from the decay time, Γ, by the slope of the Γ *versus* q^2 plot can lead to the hydrodynamic radius R_h by the Stokes–Einstein equation $R_h = k_B T/(6\pi\eta D)$, where k_B, T, and η are the Boltzmann constant, the absolute temperature, and the solvent viscosity, respectively.

The static light scattering (SLS) measurements gave the root-mean-square z-average radius of gyration ($\langle R_g \rangle$), which reflected the density distribution of the chain in real physical space. In SLS, the angular dependence of the excess absolute time-average scattered intensity, *i.e.* the Rayleigh ratio $R_{vv}(q)$ of the dilute dispersion, leads to R_g.

Ca^{2+} electrode measurements. The Ca^{2+} activity in the mineralization solution was recorded using a Ca^{2+} selective electrode (REX PCa-1-01) in conjunction with a reference electrode (REX 232-01). Before measurements, the electrodes were calibrated with $CaCl_2$ solutions of known concentrations (0.1–15 mM). The activity of Ca^{2+} was recorded every 2 minutes.

Thermogravimetry analysis (TG). TG was performed using a thermogravimetric analyzer (NETZSCH STA 409 PC/PG) under nitrogen flow at a heating rate of 10 °C min^{-1} from room temperature to 800 °C.

Elemental analysis. The fraction of polymers in reaction intermediates was measured *via* elemental (C/H/N) analysis using elementar vario EL III. The GPG content could be calculated *via* the amount of nitrogen.

Results

Characterization of PLGA-*b*-PPO-*b*-PLGA self-assemblies

PPO blocks can be dissolved in aqueous solution at 5 °C. While temperature increases, the PPO blocks become insoluble and the copolymers self-assemble into aggregates.[22,48] Turbidity measurement was employed to characterize the temperature-induced self-assembly behaviour of the copolymers. As shown in Fig. 1a, the self-assembly occurs at around 15 °C, as indicated by the abrupt increase in turbidity.[49] TEM and SEM results reveal that the copolymers form vesicles at a pH value of 5.0 in the temperature range of 20–50 °C, which is in accordance with our previous work.[22] Fig. 1b and c show typical TEM and SEM images of GPG61 vesicles prepared at 50 °C. The vesicle structure is illustrated in Fig. 1d. The PPO chains form the wall and the PLGA blocks form the corona of the vesicles.

The structure of the vesicles was further investigated by laser light scattering and electrophoresis testing (Table 2). The $\langle R_h \rangle$ value of GPG61 vesicles at 50 °C with a concentration of

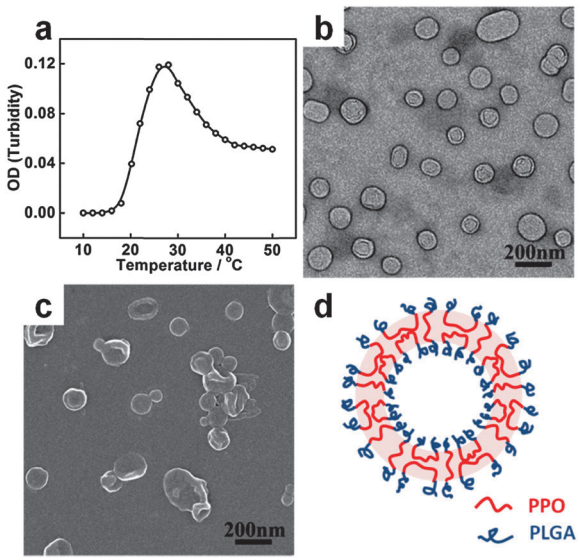

Fig. 1 (a) Turbidity (optical density) curve of GPG61 solution as a function of temperature. (b) TEM and (c) SEM images of GPG61 vesicles self-assembled by GPG61 at 50 °C. [GPG61] = 1.0 g L^{-1}. The sample was prepared by placing a drop of solution on a film-coated copper grid and quickly freezing the solution by liquid nitrogen before drying in a vacuum. (d) Schematic presentation of the GPG vesicle structure.

1.0 g L^{-1} is 111 nm with a narrow distribution. Increase in the $\langle R_h \rangle$ value and the size distribution was observed when decreasing the temperature from 50 to 20 °C, which are related to the higher hydration degree of the PPO blocks together with the more rapid chain exchange between vesicles and free chains.[22,46,48] The size of the vesicles also increases with copolymer concentration due to the larger aggregation number of copolymers in vesicles.[49–51] The $\langle R_h \rangle$ values of GPG36 and GPG124 vesicles at 50 °C with a concentration of 1.0 g L^{-1} are 118 and 109 nm, respectively, which indicate that the sizes of vesicles with different PLGA block lengths are similar under this experimental condition. The $\langle R_g \rangle / \langle R_h \rangle$ values of the aggregates prepared at various conditions are around 1, which can be attributed to the vesicle geometry.[52] Additionally, the vesicles possess anionic surfaces, as indicated by the negative zeta potentials.[53] It should be noted that the addition of Ca^{2+} cannot change the structure of vesicles. But the size of vesicles slightly increases due to the binding of Ca^{2+} with PLGA chains, as indicated by the higher zeta potentials of GPG-Ca^{2+} vesicles with Ca^{2+}.[54] More details of the GPG-Ca^{2+} vesicles are provided in the ESI† (Table S1).

Table 2 Characteristics of PLGA-*b*-PPO-*b*-PLGA copolymer vesicles

Copolymer	Conc./ g L^{-1}	Temp./°C	$\langle R_h \rangle$/nm	PDI[a]	$\langle R_g \rangle$/nm	$\langle R_g \rangle / \langle R_h \rangle$	ξ/mV
GPG61	1.0	50	111.2	0.09	105.7	0.95	−36.5
GPG61	1.0	35	149.2	0.12	159.3	1.07	−35.6
GPG61	1.0	20	196.6	0.13	206.5	1.05	−34.7
GPG61	0.5	50	82.9	0.06	86.6	1.04	−34.1
GPG61	1.5	50	174.8	0.10	168.2	0.96	−40.9
GPG36	1.0	50	118.2	0.10	117.6	0.99	−31.7
GPG124	1.0	50	109.9	0.11	106.5	0.97	−38.1

[a] Polydispersity index (PDI) of the vesicles was determined at the scattering angle of 90°.

Effect of vesicles with different PLGA block lengths on $CaCO_3$ mineralization

The effect of GPG vesicles with different PLGA block lengths on mineralization was studied first. Fig. 2 shows SEM images of $CaCO_3$ precipitates obtained in the presence of GPG36, GPG61, and GPG124 vesicles at 50 °C. All the formed crystals exhibit an overall morphology of coral-like clusters. The cluster structures are constructed from fibres which appear to grow off underlying crystal patches. Most fibres are not straight and grow in a serpentine fashion. The diameter of fibres increases from about 100 nm (GPG36, Fig. 2a and b) to 400 nm (GPG61, Fig. 2c and d) and 1 μm (GPG124, Fig. 2e and f) with the length of the PLGA block.

The crystal structure of the fibres was examined by TEM and SAED (Fig. 3). TEM analysis clearly reveals the increase of the fibre diameter with the PLGA block length (Fig. 3a–c). These fibres are composed of approximately 10 nm nanoparticles (Fig. 3d). SAED results of the fibres yield spot patterns of single crystals (insets in Fig. 3a–c). The single-crystalline diffraction patterns can be caused by good alignment of the fibre

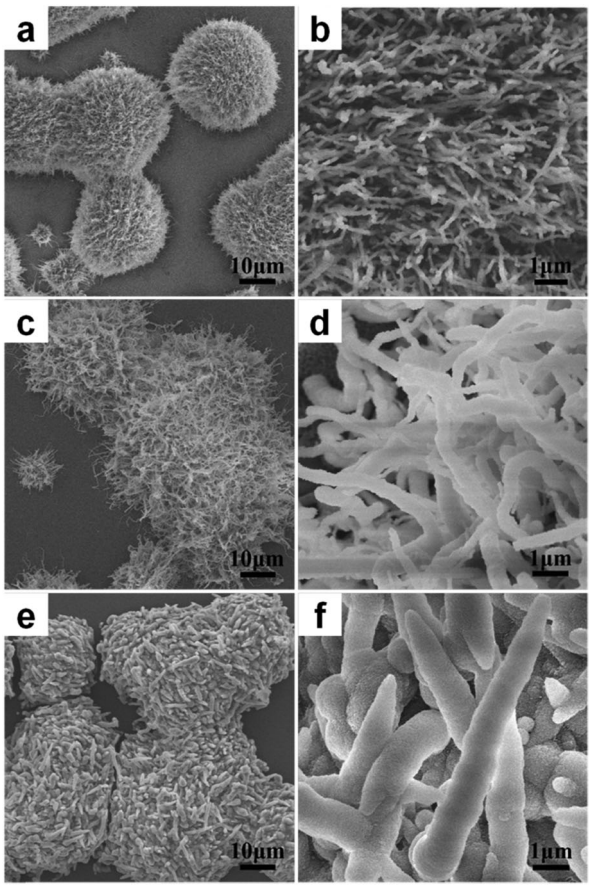

Fig. 2 SEM images of $CaCO_3$ crystals obtained at 50 °C in the presence of GPG vesicles with different PLGA chain lengths. (a and b) GPG36; (c and d) GPG61; (e and f) GPG124. [Ca^{2+}] = 15 mM, [GPG] = 1.0 g L^{-1}.

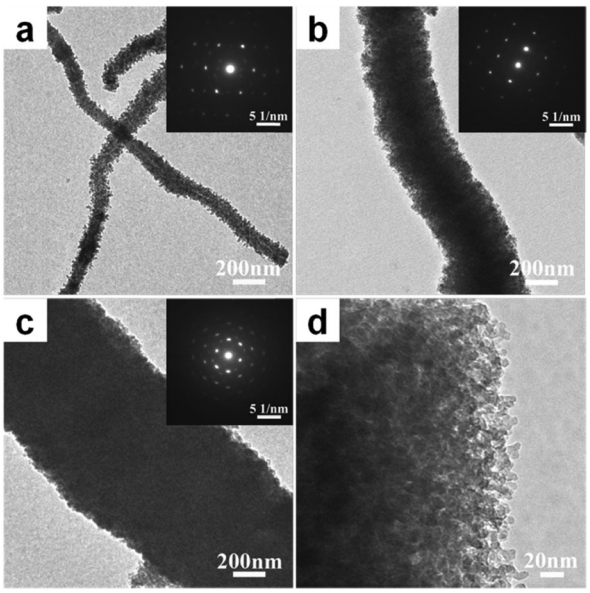

Fig. 3 TEM images of fibres obtained at 50 °C in the presence of GPG vesicles with different PLGA chain lengths. (a) GPG36; (b) GPG61; (c) GPG124; (d) magnified picture of Fig. 4b. Insets in Fig. 4a–c are the corresponding SAED patterns of the fibres. [Ca^{2+}] = 15 mM, [GPG] = 1.0 g L^{-1}.

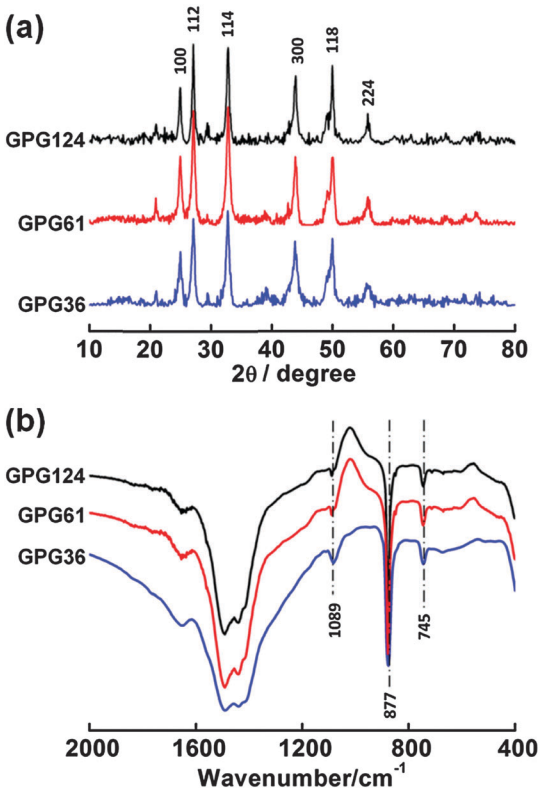

Fig. 4 (a) XRD and (b) FTIR patterns of the $CaCO_3$ crystals prepared in the presence of GPG36, GPG61, and GPG124 vesicles at 50 °C. [Ca^{2+}] = 15 mM, [GPG] = 1.0 g L^{-1}.

nanocrystalline domains along the fibre. Such nanostructured single crystals have been described as mesocrystals.[55,56]

The structure of the $CaCO_3$ fibres was further examined by XRD and FTIR (Fig. 4). The three samples display similar XRD patterns. As shown in Fig. 4a, XRD patterns of the crystals exhibit sharp reflections at 0.357, 0.329, 0.273, 0.206, 0.182, and 0.165 nm, which are consistent with the (100), (112), (114), (300), (118), and (224) reflections of vaterite.[28] No peak assigned for calcite and aragonite can be found, indicating that the three samples are pure vaterite. The results were confirmed by FTIR spectra. The presence of 1089 cm^{-1} (ν1 mode), 877 cm^{-1} (ν2 mode), and 745 cm^{-1} (ν4 mode) CO_3^{2-} absorption bands suggests the existence of only the vaterite phase (Fig. 4b).[57]

The mineralization of $CaCO_3$ at various temperatures

We consider GPG61, for example, to examine the effect of temperature on $CaCO_3$ crystallization. Fig. 5 shows the SEM and TEM images of crystals obtained under the mediation of GPG61 at 35, 20, and 5 °C. The results are compared with those obtained at 50 °C. As discussed above, the vesicles become larger with decrease in temperature from 50 to 20 °C. The structure of $CaCO_3$ fibres was also found to change within this temperature range. At 50 °C, long fibres with uniform diameter from roots to tips are formed (Fig. 2c and d). At 35 °C, straight spines with relatively thick roots and sharp tips are formed on spherical particles (Fig. 5a and b). At 20 °C, the spines become more tapered and shorter, exhibiting a cone-like morphology (Fig. 5c and d). These spines show a single-crystalline structure that is comprised of nanocrystalline domains, as indicated by the spotty SAED patterns. By further decreasing the temperature to 5 °C, the PPO blocks can be dissolved and the vesicles are dissociated. Under this condition, $CaCO_3$ smooth spheres are formed (Fig. 5e). The spheres are single crystals containing an internal fibro texture (Fig. 5f). In the cases of GPG36 and GPG124, the structural evolution of fibres with temperature shows the same tendency as GPG61.

Polymorphs of the crystals prepared at various temperatures were examined by XRD and FTIR measurements (Fig. 6). In FTIR spectra, the absorption bands at 745 and 712 cm^{-1} can be attributed to ν4 (in-plane bending mode) bands of vaterite and calcite, respectively.[57] At 35 and 20 °C, the polymorphs are indexed as a mixture of calcite and vaterite. However, at 20 °C, the peaks of vaterite are less evident and the peaks of calcite are stronger, which suggests that the vaterite content is lower than that at 35 °C. By further decreasing the temperature to 5 °C, peaks assigned for only calcite can be seen, indicating that the crystals are pure calcite. As mentioned above, the crystals formed at 50 °C are pure vaterite. Thus, the polymorph tends to be calcite at lower temperature and the formation of vaterite is favoured at higher temperature.

As control experiment, $CaCO_3$ crystallization in the presence of PLGA or PPO homopolymers at various temperatures was examined. Under the mediation of PLGA homopolymer, spherical crystals with a smooth surface are generated. The polymorphs were found to be pure vaterite at temperatures ranging from 50 to 5 °C. While mediated by PPO homopolymer, rhombohedra calcite crystals which are similar to the crystals formed without polymer additives are produced. The results indicate

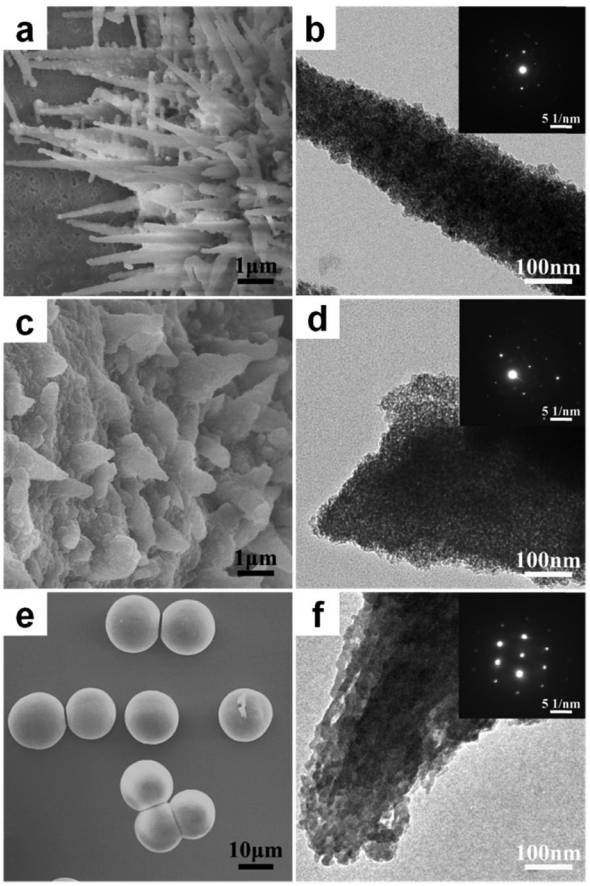

Fig. 5 SEM and TEM images of $CaCO_3$ crystals formed in the presence of GPG61 at different temperatures: (a and b) 35 °C; (c and d) 20 °C. (e and f) 5 °C. $[Ca^{2+}]$ = 15 mM, [GPG61] = 1.0 g L^{-1}. Insets are the SAED patterns.

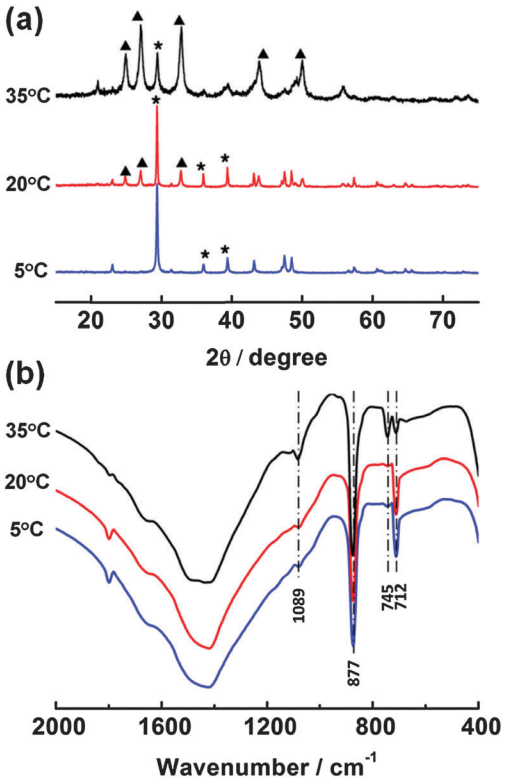

Fig. 6 (a) XRD and (b) FTIR patterns of the $CaCO_3$ crystals prepared in the presence of GPG61 at 35, 20, and 5 °C. $[Ca^{2+}]$ = 15 mM, [GPG61] = 1.0 g L^{-1}. Note: "▲" denotes vaterite (JCPDS: 33-0268) and "☆" denotes calcite (JCPDS: 47-1743).

that the homopolymer directed $CaCO_3$ crystallization is independent of temperature (Fig. S3 and S4, ESI†).

Effect of initial Ca^{2+} and copolymer concentrations on the crystal morphology

The mineralization behaviour at various initial concentrations of Ca^{2+} (10, 15, 20 mM) and the polymer (0.5, 1.0, 1.5 g L^{-1}) was further investigated (experimental temperature was fixed at 50 °C). As shown in Fig. 7, the overall morphology of crystals depends on initial Ca^{2+} concentration. At lower Ca^{2+} concentration (10 mM), the crystals show a rosette-like morphology which is constructed from spherical crystalline units (Fig. 7a–c). When Ca^{2+} concentration is increased to 15 mM and 20 mM, long fibre clusters are formed (Fig. 7d–i). These results indicate that the formation of $CaCO_3$ fibres requires higher Ca^{2+} concentration. Moreover, the diameter of $CaCO_3$ fibres was found to be determined by the polymer concentration. For example, at 15 mM Ca^{2+} concentration, the fibre diameter increases dramatically from *ca.* 200 nm at 0.5 g L^{-1} GPG61 to *ca.* 700 nm at 1.5 g L^{-1} GPG61 (Fig. 7d–f). In the cases of GPG36 and GPG124, such a tendency was also observed. Fig. 8 shows the statistic results of fibre diameters as a function of the copolymer concentration. Each data were collected from more than 100 fibres. The increase of the fibre diameter with copolymer concentration can be observed in a wide range of copolymer concentrations from 0.1 to 2.0 g L^{-1}.

The formation process of fibres

Inorganic fibres can be produced through several mineralization methods, *e.g.* the direct-aggregation process,[37,58,59] oriented attachment,[36] site-selective growth,[60] and solution–precursor–solid process.[40,61] To clarify the mechanism of fibre formation in this work, the mineral structures at various reaction intervals were monitored. First, the decay of free Ca^{2+} (*i.e.* Ca^{2+} that are neither bound to polymers nor involved in $CaCO_3$ formation) with time was recorded to gain information about the mineralization process at 50 °C (black line in Fig. 9). A plateau was observed in the evolution of Ca^{2+} activity (as indicated by the black arrow), which was evidence for the formation of a temporarily stabilized phase.[62,63] Thus, the mineralization process at 50 °C could be divided into three stages. In the first stage, the Ca^{2+} activity decreased dramatically due to the formation of an intermediate phase. In the second stage, the activity of Ca^{2+} reached a relatively constant level as a result of the stabilization of the intermediates. In the third stage, the Ca^{2+} activity dropped again, suggesting the transformation of the intermediate phase.

The formation and transformation of the intermediate phase in the three stages of the reaction were then monitored by TEM. At 15 min, small amorphous particles were observed in the aqueous cavity of the vesicles (Fig. 10a). The particles were

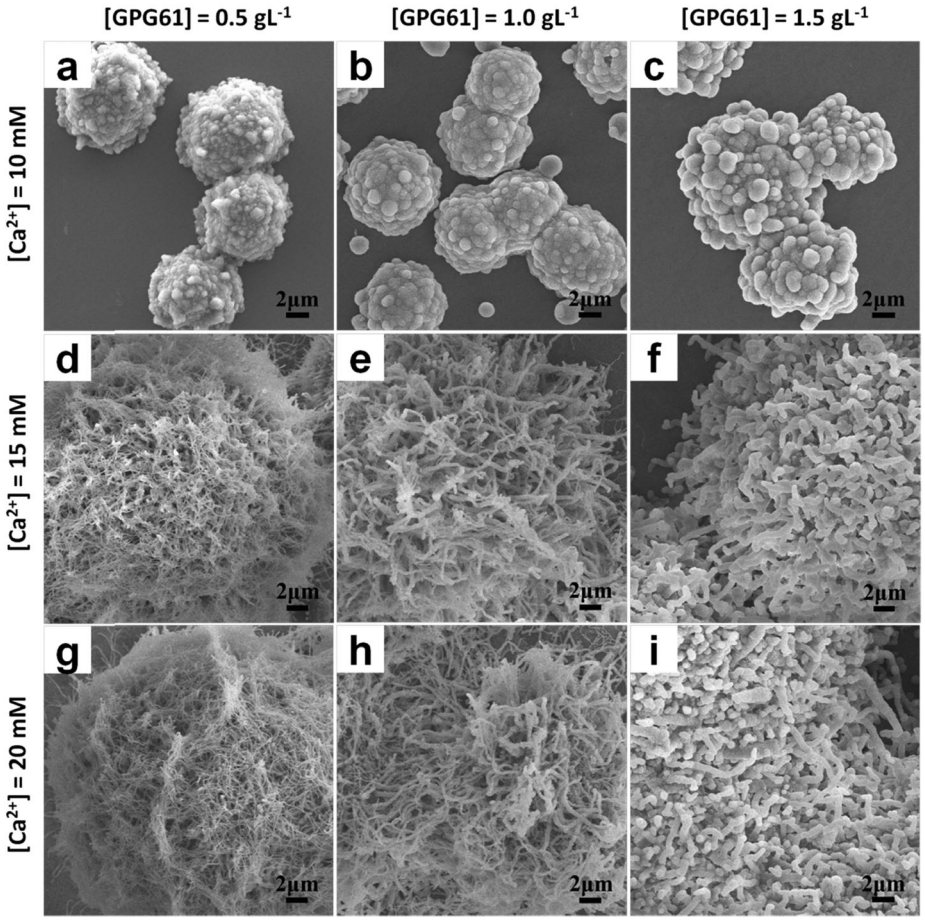

Fig. 7 SEM images of $CaCO_3$ crystals obtained with various initial Ca^{2+} and GPG61 concentrations at 50 °C. (a) [GPG61] = 0.5 g L^{-1}, [Ca^{2+}] = 10 mM; (b) [GPG61] = 1.0 g L^{-1}, [Ca^{2+}] = 10 mM; (c) [GPG61] = 1.5 g L^{-1}, [Ca^{2+}] = 10 mM; (d) [GPG61] = 0.5 g L^{-1}, [Ca^{2+}] = 15 mM; (e) [GPG61] = 1.0 g L^{-1}, [Ca^{2+}] = 15 mM; (f) [GPG61] = 1.5 g L^{-1}, [Ca^{2+}] = 15 mM; (g) [GPG61] = 0.5 g L^{-1}, [Ca^{2+}] = 20 mM; (h) [GPG61] = 1.0 g L^{-1}, [Ca^{2+}] = 20 mM; (i) [GPG61] = 1.5 g L^{-1}, [Ca^{2+}] = 20 mM.

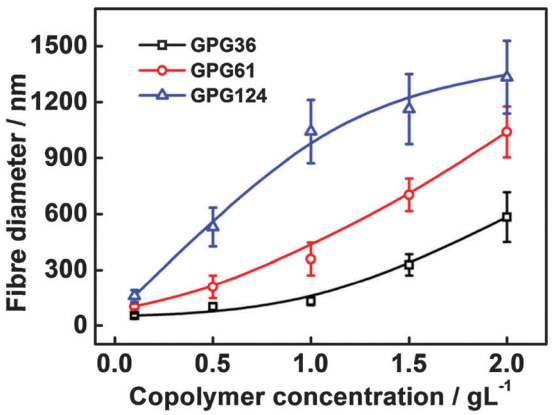

Fig. 8 Diameters of $CaCO_3$ fibres as a function of copolymer concentration at 50 °C. [Ca^{2+}] = 15 mM.

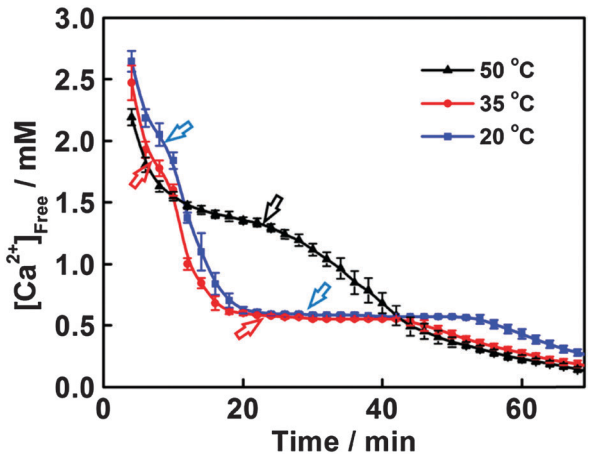

Fig. 9 Evolution of Ca^{2+} activity with time at 50, 35, and 20 °C. Initial [Ca^{2+}] = 15 mM, [GPG61] = 1.0 g L^{-1}. Error bars depict standard deviations of three replicas of measurements. Arrows show the plateaus in evolution.

formed in the vesicle corona, as well, which prevented the collapse of vesicles and resulted in the non-spherical shape of vesicles. After reaction for 30 min, large liquid-like amorphous particles were obtained and some of the particles still maintained the shape of the vesicles (Fig. 10b). These particles are similar to the liquid amorphous mineral emulsions observed in Wolf's work,

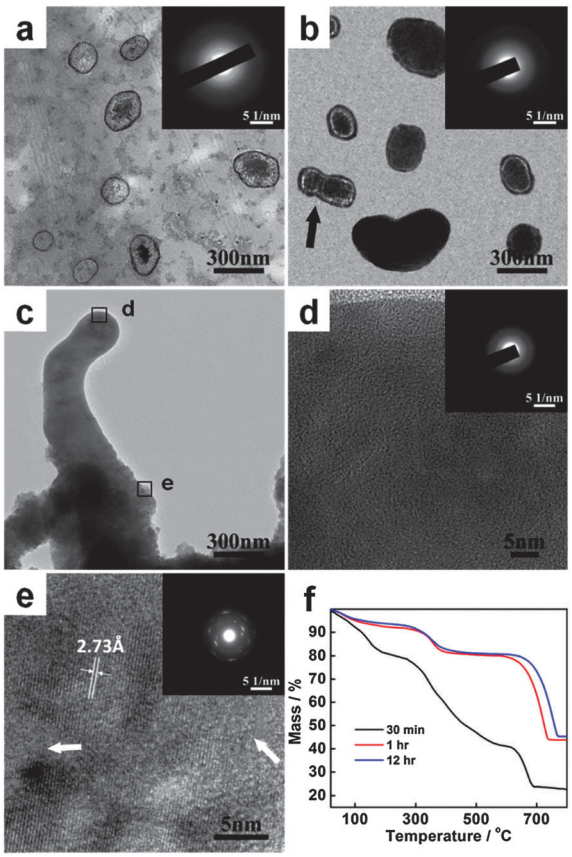

Fig. 10 TEM-SAED and TG analysis of mineralizaiton intermediates at different reaction intervals under the mediation of GPG61 vesicles at 50 °C (a) amorphous phase formed within 15 min of reaction. (b) Liquid-like precursor particles formed after reaction for 30 min. (c) Fibrous crystals formed after reaction for 60 min. (d) HR-TEM image of the top area of the fibre. (e) HR-TEM image of the bottom area of the fibre. Insets are the SAED patterns. (f) TG traces of intermediates collected at 30 min, 1 h, and 12 h. The first weight loss was assigned for the water release (from beginning to 200 °C), and the second loss was the decomposition of GPG (200–600 °C). [Ca^{2+}] = 15 mM, [GPG61] = 1.0 g L^{-1}.

where the low contrast variation inside of the particles was claimed to be a proof of their liquid-like state.[64] Further support for their liquid state is the coalescence behaviour of the particles (as indicated by the arrow in Fig. 10b). The obvious coalescence behaviour of the liquid-state particles is also shown in Fig. S5a (ESI†). At 60 min, fibres were formed with colloidal-like "bobbles" on the tip (Fig. S5b, ESI†). A typical fibre is shown in Fig. 10c. The crystallographic nature of the top and bottom areas of the fibre was examined by HR-TEM and SAED. The absence of lattice fringes in the top area of the fibre indicates the amorphous state, which was confirmed by the diffuse scattering SAED pattern (Fig. 10d). In addition, the liquid-like tip quickly shrank and distorted under the focused electron beam during observation, indicating the unstable amorphous structure. However, nanocrystalline domains with 2.73 Å lattice fringes could be observed in the bottom area, which were separated by amorphous interstices (as indicated by the arrows in Fig. 10e). The SAED analysis showed arc diffraction patterns, indicating a polycrystalline structure with high crystallographic orientation.

The above mineralization process shows the characteristic features of the solution–precursor–solid (SPS) mechanism: (1) the formation of a liquid state precursor in the initial stage of the reaction, and (2) drop-like amorphous growth points at the tip of the fibres. In the SPS process, a "molten flux droplet" is created from the polymer-induced liquid-precursor (PILP) droplets and then grows in an autocatalytic way to form one-dimensional morphologies.[61] Here, the PILP droplets were aggregates of liquid-like precursor particles.[61] To further examine the behaviour of the vesicles in mineralization, we measured the fraction of polymers in mineralization intermediates by means of TG and elemental analysis (Table 3 and Fig. 10f). At 30 min, the PILP phase comprised about 40 wt% polymer. The remarkably high polymer content in the PILP phase confirmed the incorporation of vesicles into amorphous precursors. However, the polymer contents in precipitated crystals at 1 h and 12 h decreased to around 17 and 14 wt%, respectively. The dramatic decrease of the polymer content in crystals indicated the extrusion of vesicles during crystallization. Additionally, the water content in the PILP phase at 30 min was relatively higher. The decrease of water content with time indicated the transformation from the hydrated amorphous phase to anhydrous crystals.

In this work, the diameter of the fibre was found to be dependent on the polymer concentration and copolymer block composition. Since the diameter of the fibre is limited to the size of PILP droplets in the SPS process, it is assumed that the variation in the fibre diameter was caused by the different aggregation behaviour of vesicle-precursor particles. To verify this speculation, the development of amorphous precursors in GPG36, GPG61, and GPG124 vesicle solution in the early stage of mineralization was monitored by dynamic light scattering. As shown in Fig. 11, the R_h values and distributions of precursors increased with time in all solutions, indicating that the liquid precursors were formed through an aggregation process of vesicle-precursor particles. Within 15 min, the sizes of vesicle-precursor particle agglomerates were similar in the three solutions. As mineralization proceeds, the R_h values of the particle agglomerates started to be considerably different.

Table 3 Composition analysis of intermediates at different time intervals

Temp. (°C)	Time (h)	GPG content[a] (wt%)	GPG content[b] (wt%)	Water content[c] (wt%)
50	0.5	40.1	40.9	18.1
	1	17.3	12.8	8.2
	12	14.3	11.0	7.6
35	0.5	33.9	34.1	10.0
	1	11.6	12.0	5.7
	12	10.8	10.3	4.9
20	0.5	27.0	28.7	5.2
	1	9.6	9.8	4.5
	12	7.4	9.6	2.6

[a] The weight fraction of polymers in the third column was calculated from the amount of nitrogen in elemental analysis. [b] The weight fraction of polymers in the fourth column was estimated from the second weight loss process in TG analysis. [c] The weight fraction of water was estimated from the first weight loss process in TG analysis.

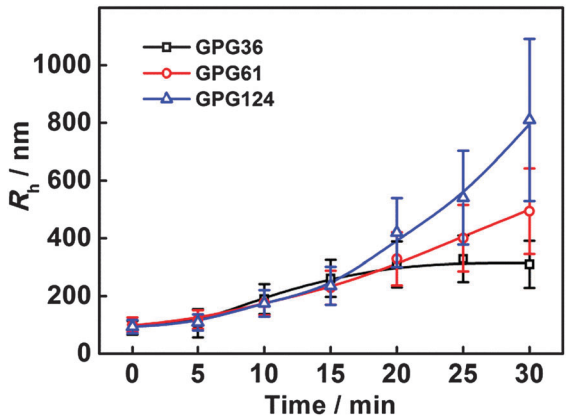

Fig. 11 Evolution of the hydrodynamic radius of particles during the initial reaction period in the solution of GPG36, GPG61, and GPG124 vesicles at 50 °C. The R_h value was measured by DLS at a fixed angle of 90°. The error bars are the standard deviations of R_h distributions. [Ca^{2+}] = 15 mM, [GPG] = 1.0 g L^{-1}.

It could be seen that the R_h value increased faster when the PLGA length was longer, which indicated that the vesicle-precursor particles were more inclined to aggregate with each other. This tendency is in accordance with the dependence of the fibre diameter on the PLGA length of copolymers (Fig. 2). It should be mentioned that the size of particle agglomerates in solution is larger than the fibre diameter due to the dehydration and shrinking of the amorphous phase during crystallization. The results demonstrate that the fibre diameter variation is caused by the different aggregation behaviours of vesicle-precursor particles. This mechanism can also be used to explain the influence of copolymer concentration on the diameter of $CaCO_3$ fibres. With more copolymer vesicles in the solution, the generated vesicle-$CaCO_3$ particles are more likely to aggregate and form larger agglomerates.

The formation process of spines at lower temperatures was also studied by examining the mineralization intermediates at different reaction intervals. The decay of free Ca^{2+} at 35 and 20 °C was first studied. The evolution exhibited two plateaus (as indicated by the blue and red arrows in Fig. 9), which was a sign that the mineralization went through more than one phase transformation process. Fig. 12 displays the TEM images of intermediates at different reaction times at 35 and 20 °C. After 15 min reaction, liquid-like amorphous precursors were observed at both temperatures. Most of the precursor particles were formed in bulk solution and connected with vesicles (Fig. 12a and e). After 30 min, the amorphous particles started to show a solid-like morphology (Fig. 12b and f). Some of the particles were hollow (as indicated by the arrow), which were caused by the dissolution of the particles from inside. TG and elemental analysis revealed that the polymer and water contents in these amorphous particles were lower than that at 50 °C, indicating that fewer vesicles were incorporated into particles at lower temperature (Table 3 and Fig. 12d and h). After 1 h, spines composed of nanoparticles could be observed. The ring SAED patterns of the spines indicated the polycrystalline structure (Fig. 12c and g). Based on the fact that some amorphous particles were dissolved and the crystallization occurred in precipitate-free circular halos (Fig. S5d, ESI†), the spines were formed from the dissolution and recrystallization process of amorphous particles. The polycrystalline structure was attributed to the random distribution of nanoparticles, which could reorder during phase transformation to form the final single crystals.

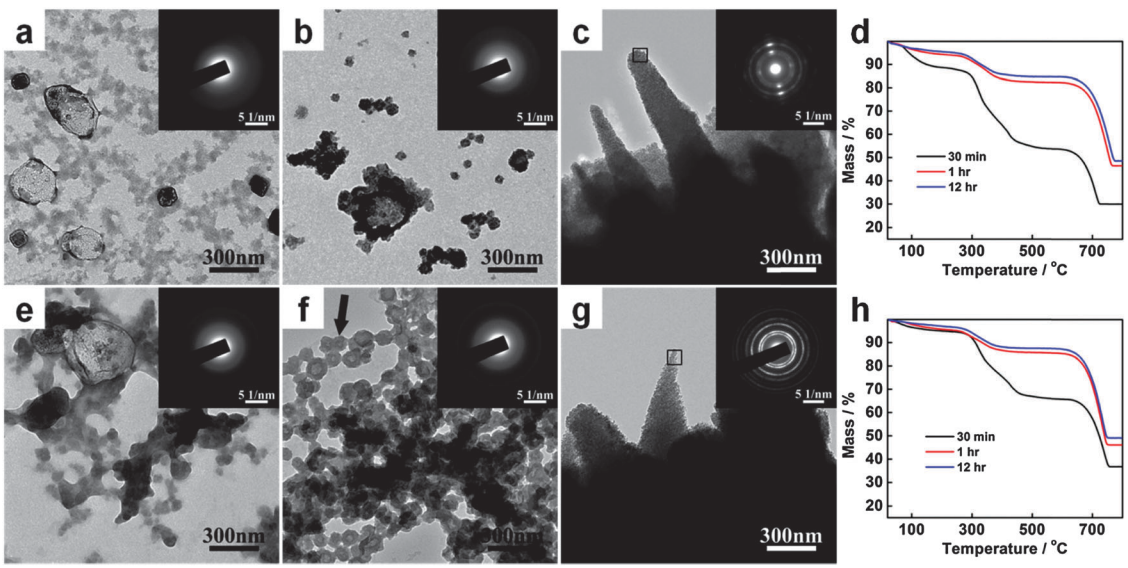

Fig. 12 TEM-SAED and TG analysis of mineralization intermediates at different reaction intervals under the mediation of GPG61 vesicles at 35 (a–d) and 20 °C (e–h). (a and e) Amorphous phase was formed within 15 min of reaction. (b and f) Solid amorphous particles formed after reaction for 30 min. (c and g) Spines formed after reaction for 60 min. Insets are the SAED patterns of the marked areas. (d and h) TG traces of intermediates collected at 30 min, 1 h, and 12 h. The first weight loss was assigned for the water release (from beginning to 200 °C), and the second loss was the decomposition of GPG (200–600 °C). [Ca^{2+}] = 15 mM, [GPG61] = 1.0 g L^{-1}.

It can be seen that the crystallization process at lower temperature is distinct from that at higher temperature. First, more amorphous precursors are formed in bulk solution than in the vesicles. Second, the liquid amorphous phase transforms into the solid state before crystallization (which was also confirmed by SEM, Fig. S5, ESI†). Third, crystallization goes through the dissolution and recrystallization pathway. We believe that these differences are attributed to the role of vesicles in the formation of amorphous particles. At lower temperature, the vesicles act as absorbates on amorphous particles rather than templates. Thus, the vesicles cannot effectively stabilize amorphous precursors, resulting in the solidification of hydrate precursors and the dissolution of solid precursors.

Discussion

Fibre is an intriguing morphology, whose formation process has attracted much attention. In applied science, the fibrous architecture provides mechanical properties well suited for friction and vibration. In terms of fundamental science, fibre formation does not follow crystallographic symmetry. The formation mechanism can provide useful information for non-classical crystallization theory. In a number of previous studies, $CaCO_3$ fibres or fibre-like structures such as whiskers and rods have been produced through the use of soluble additives (polyacid block copolymers[65] and cationic polyelectrolytes[66]) or insoluble matrixes (microemulsion[67,68] and hard template[69]). These additives act either as crystal growth modifiers or nucleation templates.

From the experimental results, we discovered that $CaCO_3$ fibres can be formed under the mediation of PLGA-*b*-PPO-*b*-PLGA vesicles. The investigation of the mineralization process reveals that the GPG vesicles play a key role in the formation of amorphous precursors. At higher temperature, the GPG vesicles play two roles: (1) the PLGA blocks can concentrate ionic species and delay the nucleation of $CaCO_3$;and (2) the vesicle wall composed of PPO blocks provides a ''confined template'' for the formation of an amorphous phase. At lower temperature, the vesicles act as absorbates on the amorphous phase rather than the template. Based on the experimental results and the above analyses, a proposed mechanism for the vesicle-induced formation of fibres is represented in Scheme 1. In the first stage of mineralization, ionic species are sequestered and concentrated in the vesicle corona (Scheme 1a). At lower Ca^{2+} concentration, the effect of carboxyl groups on sequestering Ca^{2+} is restrained, which leads to the formation of rosette-like crystals (Fig. 7b).

As the reaction proceeds, amorphous calcium carbonate (ACC) particles are formed through different pathways depending on the temperature. At lower temperature, it is revealed that vesicles are relatively larger due to the higher hydration degree of PPO segments. These vesicles with loose structures cannot effectively confine and stabilize the hydrated amorphous precursors. Thus, most of the precursors are formed in bulk solution (Scheme 1b and Fig. 12e). The precursors then exclude water molecules and show the features of solid particles (Scheme 1c and Fig. 12f). Due to the instability of the solid amorphous particles, they are finally dissolved from the core and recrystallized to form spines (Scheme 1d and Fig. 12g). At higher temperature, according to the characterization of GPG vesicles, the PPO segments in vesicles are more dehydrated. Therefore, the hydrated amorphous particles formed in the vesicle cavity are stabilized, because the exchange of water molecules between amorphous particles and bulk solution is limited by the vesicle wall. Meanwhile, the amorphous particles formed outside the vesicles are dissolved due to their instability, and then serve as a source of ionic species for the growth of amorphous particles in the vesicles. As a result, the vesicle-precursor particles are generated (Scheme 1e and Fig. 10a). With mineralization continuing, the vesicle-precursor particles aggregate to form

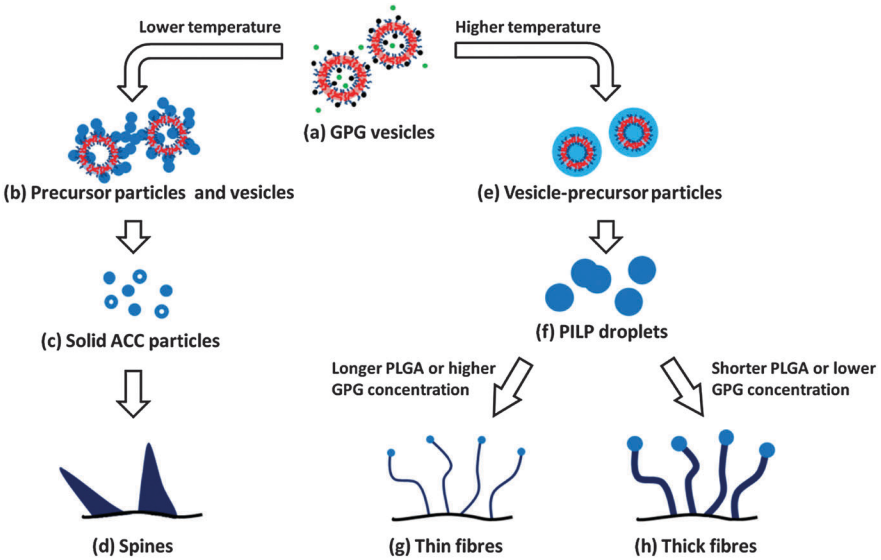

Scheme 1 A schematic image showing the crystallization routes of $CaCO_3$ mediated by GPG vesicles.

liquid-like agglomerates, which can be identified as PILP droplets (Scheme 1f and Fig. 10b). The higher fluidity of PILP droplets is favoured for the generation of a high energy site, leading to an autocatalytic effect for the preferential adsorption of droplets at the tip of fibres. Consequently, the growth of fibres is restricted to one-dimension *via* the SPS process (Fig. 10c). During the process, the diameter of fibres is influenced by the copolymer concentration and the PLGA chain length in copolymers. The shorter PLGA chain length reduces the interaction between the vesicle-precursor particles and the lower GPG concentration decreases the chance for the collision of the particles. Under this condition, PILP droplets have smaller sizes and the formed fibres have smaller diameters (Scheme 1g, Fig. 2b and 7d). In contrast, with a higher vesicle concentration and a longer PLGA chain length, the droplets are larger and the fibres have larger diameters (Scheme 1h, Fig. 2f and 7f).

The transformation of the $CaCO_3$ polymorph at different temperatures was investigated by FT-IR (Fig. S6, ESI†). At higher temperature, the crystals transformed from amorphous to vaterite, and the vaterite was stabilized as the final crystal phase. However, at lower temperature, the amorphous phase first transformed into vaterite, then the vaterite phase gradually disappeared and calcite was formed. To investigate the role of GPG copolymers in these polymorph transformation processes, we examined the polymorphs of the crystals formed in the absence of additives at various temperatures. It was found that only calcite can be formed between 5 and 50 °C (Fig. S7, ESI†). Therefore, in the work, the polymorphs are determined by the copolymers rather than temperature. At higher temperature, the crystallization of the amorphous phase occurs with the polymer acting as a surface stabilizer.[70] Therefore, the vaterite is efficiently stabilized against recrystallization. However, at lower temperature, fewer polymers are incorporated in the crystallized vaterite phase. Thus, the vaterite is unstable and recrystallizes to form a more stable calcite phase.

As discussed above, the structure of fibres is determined by the fluidity and the size of the transient amorphous precursors. We found that these two properties of the amorphous phase are closely related to the structure of the vesicles. When the PPO chains in vesicle walls are dehydrated, the vesicles can supply a confined aqueous environment for the stabilization of more hydrated precursor particles. In addition, the length of the PLGA chain in coronas can affect the interaction between vesicle-precursor particles. As a result, the fluidity and size of the amorphous phase are regulated by the structure of polypeptide vesicles. It can be expected that by using polypeptide vesicles as a crystallization template for the amorphous phase, more inorganic biomimetic materials with highly regulated structures can be produced.

Conclusions

In this work, we reported the mineralization of $CaCO_3$ mediated by PLGA-*b*-PPO-*b*-PLGA polypeptide vesicles. $CaCO_3$ fibres were obtained, and the structure of fibres can be regulated by temperature, the PLGA block length in copolymers, copolymer concentration, and Ca^{2+} concentration. It was found that the growth of fibres occurred through the SPS pathway. The diameter variation of fibres is caused by the different aggregation behaviour of precursor particles. The shorter and more tapering spines are formed *via* the dissolution and recrystallization process of the solid amorphous phase. The results reveal that polypeptide vesicles are effective modifiers for biomimetic mineralization. We suggest that in the polypeptide vesicle mediated mineralization, the vesicles can concentrate and confine the amorphous phase and then regulate its aggregation and transformation behaviours. These results may help to explain the vesicle-induced formation of a highly regulated inorganic structure in organisms.

Acknowledgements

This work was supported by National Natural Science Foundation of China (21234002, 51303055, and 21474092), and National Basic Research Program of China (2012CB933600). Support from Projects of Shanghai municipality (15QA1401400, 15ZZ028, and 13JC1402000) and Fundamental Research Funds for the Central Universities (22A201514001) is also appreciated.

References

1 C. Cheng, Z. Shao and F. Vollrath, *Adv. Funct. Mater.*, 2008, **18**, 2172–2179.
2 F. Nudelman and N. Sommerdijk, *Angew. Chem., Int. Ed.*, 2012, **51**, 6582–6596.
3 X. Fei, W. Li, Z. Shao, S. Seeger, D. Zhao and X. Chen, *J. Am. Chem. Soc.*, 2014, **136**, 15781–15786.
4 S. Kim and C. B. Park, *Adv. Funct. Mater.*, 2013, **23**, 10–25.
5 G. Zhang, R. Huang, Z. Li, X. Yang, X. Chen, W. Xia, X. Sun, G. Yang, C. Gao and Z. Gou, *J. Inorg. Biochem.*, 2012, **113**, 1–8.
6 S. Wang, Y. Shu, B. Liang, L. Gao, M. Gao, P. Yin and L. Guo, *Chin. J. Polym. Sci.*, 2014, **32**, 675–680.
7 S. Raz, P. C. Hamilton, F. H. Wilt, S. Weiner and L. Addadi, *Adv. Funct. Mater.*, 2003, **13**, 480–486.
8 E. S. Vasquez, J. L. Cunningham, J. B. McMahan, C. L. Simpson and K. B. Walters, *J. Mater. Chem. B*, 2015, **3**, 6411–6419.
9 A. Schulz, H. Wang, P. van Rijn and A. Böker, *J. Mater. Chem.*, 2011, **21**, 18903–18918.
10 Y. Cai and J. Yao, *Nanoscale*, 2010, **2**, 1842–1848.
11 S. Gayathri, R. Lakshminarayanan, J. C. Weaver, D. E. Morse, R. M. Kini and S. Valiyaveettil, *Chem. – Eur. J.*, 2007, **13**, 3262–3268.
12 S. Cavalli, D. C. Popescu, E. E. Tellers, M. R. J. Vos, B. P. Pichon, M. Overhand, H. Rapaport, N. A. J. M. Sommerdijk and A. Kros, *Angew. Chem., Int. Ed.*, 2006, **45**, 739–744.
13 W. Zhu, J. Lin, C. Cai and Y. Lu, *J. Mater. Chem. B*, 2013, **1**, 841–849.
14 X. H. Guo, A. W. Xu and S.-H. Yu, *Cryst. Growth Des.*, 2008, **8**, 1233–1242.

15 L. J. Dai, X. G. Cheng and L. B. Gower, *Chem. Mater.*, 2008, **20**, 6917–6928.
16 R. S. K. Lam, J. M. Charnock, A. Lennie and F. C. Meldrum, *CrystEngComm*, 2007, **9**, 1226–1236.
17 Y. Politi, J. Mahamid, H. Goldberg, S. Weiner and L. Addadi, *CrystEngComm*, 2007, **9**, 1171–1177.
18 Y. Liu, Y. J. Cui and R. Guo, *Langmuir*, 2012, **28**, 6097–6105.
19 Y. Liu, H. Mao, X. Liu, L. Qiao and R. Guo, *CrystEngComm*, 2014, **16**, 8841–8851.
20 C. Cai, L. Wang and J. Lin, *Chem. Commun.*, 2011, **47**, 11189–11203.
21 C. Cai, J. Lin, Z. Zhuang and W. Zhu, *Adv. Polym. Sci.*, 2013, **259**, 159–199.
22 C. Cai, L. Zhang, J. Lin and L. Wang, *J. Phys. Chem. B*, 2008, **112**, 12666–12673.
23 Y.-Y. Kim, K. Ganesan, P. Yang, A. N. Kulak, S. Borukhin, S. Pechook, L. Ribeiro, R. Kröger, S. J. Eichhorn, S. P. Armes, B. Pokroy and F. C. Meldrum, *Nat. Mater.*, 2011, **10**, 890–896.
24 C. L. Chen, J. Qi, J. Tao, R. N. Zuckermann and J. J. DeYoreo, *Sci. Rep.*, 2014, **4**, 6266.
25 A. W. Perriman, D. S. Williams, A. J. Jackson, I. Grillo, J. M. Koomullil, A. Ghasparian, J. A. Robinson and S. Mann, *Small*, 2010, **6**, 1191–1196.
26 X. Guo, L. Liu, W. Wang, J. Zhang, Y. Wang and S.-H. Yu, *CrystEngComm*, 2011, **13**, 2054–2061.
27 W. Zhu, C. Cai, J. Lin, L. Wang, L. Chen and Z. Zhuang, *Chem. Commun.*, 2012, **48**, 8544–8546.
28 W. Zhu, J. Lin and C. Cai, *J. Mater. Chem.*, 2012, **22**, 3939–3947.
29 A. Komeili, H. Vali, T. J. Beveridge and D. K. Newman, *Proc. Natl. Acad. Sci. U. S. A.*, 2004, **101**, 3839–3844.
30 M. Sumper, *Science*, 2002, **295**, 2430–2433.
31 J. R. Young, S. A. Davis, P. R. Bown and S. Mann, *J. Struct. Biol.*, 1999, **126**, 195–215.
32 S. Weiner, I. Sagi and L. Addadi, *Science*, 2005, **309**, 1027–1028.
33 L. B. Gower, *Chem. Rev.*, 2008, **108**, 4551–4627.
34 J. Fletcher, D. Walsh, C. E. Fowler and S. Mann, *CrystEngComm*, 2011, **13**, 3692–3697.
35 L. Lao, Y. Wang, Y. Zhu, Y. Zhang and C. Gao, *J. Mater. Sci.: Mater. Med.*, 2011, **22**, 1873–1884.
36 L. Qi, H. Cölfen, M. Antonietti, M. Li, J. D. Hopwood, A. J. Ashley and S. Mann, *Chem. – Eur. J.*, 2001, **7**, 3526–3532.
37 X. Long, Y. Ma, K. R. Cho, D. Li, J. J. De Yoreo and L. Qi, *Cryst. Growth Des.*, 2013, **13**, 3856–3863.
38 S. Kajiyama, T. Nishimura, T. Sakamoto and T. Kato, *Small*, 2014, **10**, 1634–1641.
39 M. J. Olszta, S. Gajjeraman, M. Kaufman and L. B. Gower, *Chem. Mater.*, 2004, **16**, 2355–2362.
40 S. J. Homeijer, M. J. Olszta, R. A. Barrett and L. B. Gower, *J. Cryst. Growth*, 2008, **310**, 2938–2945.
41 N. Hadjichristidis, H. Iatrou, M. Pitsikalis and J. Mays, *Prog. Polym. Sci.*, 2006, **31**, 1068–1132.
42 C. Cai, Y. Li, J. Lin, L. Wang, S. Lin, X.-S. Wang and T. Jiang, *Angew. Chem., Int. Ed.*, 2013, **52**, 7732–7736.
43 Z. Zhuang, X. Zhu, C. Cai, J. Lin and L. Wang, *J. Phys. Chem. B*, 2012, **116**, 10125–10134.
44 Y. Li, T. Jiang, S. Lin, J. Lin, C. Cai and X. Zhu, *Sci. Rep.*, 2015, **5**, 10137.
45 L. Chen, T. Chen, W. Fang, Y. Wen, S. Lin, J. Lin and C. Cai, *Biomacromolecules*, 2013, **14**, 4320–4330.
46 L. Wei, C. Cai, J. Lin and T. Chen, *Biomaterials*, 2009, **30**, 2606–2613.
47 C. C. Tester, R. E. Brock, C.-H. Wu, M. R. Krejci, S. Weigand and D. Joester, *CrystEngComm*, 2011, **13**, 3975–3978.
48 W. Agut, A. Brûlet, D. Taton and S. Lecommandoux, *Langmuir*, 2007, **23**, 11526–11533.
49 Z. Zhuang, C. Cai, T. Jiang, J. Lin and C. Yang, *Polymer*, 2014, **55**, 602–610.
50 Y. F. Wu, X. L. Liu, Y. Wang, Z. R. Guo and Y. J. Feng, *Macromol. Chem. Phys.*, 2012, **213**, 1489–1498.
51 C. Zhou, M. A. Hillmyer and T. P. Lodge, *Macromolecules*, 2011, **44**, 1635–1641.
52 W.-M. Wan, C.-Y. Hong and C.-Y. Pan, *Chem. Commun.*, 2009, 5883–5885.
53 A. Szczes, *Colloids Surf., B*, 2013, **101**, 44–48.
54 L. Zhang and A. Eisenberg, *Macromolecules*, 1996, **29**, 8805–8815.
55 R. Q. Song and H. Cölfen, *Adv. Mater.*, 2010, **22**, 1301–1330.
56 J. Seto, Y. R. Ma, S. A. Davis, F. Meldrum, A. Gourrier, Y.-Y. Kim, U. Schilde, M. Sztucki, M. Burghammer, S. Maltsev, C. Jager and H. Cölfen, *Proc. Natl. Acad. Sci. U. S. A.*, 2012, **109**, 3699–3704.
57 J. Yang, Y. H. Liu, T. Wen, X. X. Wei, Z. Y. Li, Y. L. Cai, Y. L. Su and D. J. Wang, *Cryst. Growth Des.*, 2012, **12**, 29–32.
58 Y.-Y. Kim, A. N. Kulak, Y. Li, T. Batten, M. Kuball, S. P. Armes and F. C. Meldrum, *J. Mater. Chem.*, 2009, **19**, 387–398.
59 T. Miura, A. Kotachi, Y. Oaki and H. Imai, *Cryst. Growth Des.*, 2006, **6**, 612–615.
60 M. Antonietti, M. Breulmann, C. G. Göltner, H. Cölfen, K. K. W. Wong, D. Walsh and S. Mann, *Chem. – Eur. J.*, 1998, **4**, 2493–2500.
61 S. J. Homeijer, R. A. Barrett and L. B. Gower, *Cryst. Growth Des.*, 2010, **10**, 1040–1052.
62 M. A. Bewernitz, D. Gebauer, J. Long, H. Cölfen and L. B. Gower, *Faraday Discuss.*, 2012, **159**, 291–312.
63 J. Rieger, T. Frechen, G. Cox, W. Heckmann, C. Schmidt and J. Thieme, *Faraday Discuss.*, 2007, **136**, 265–277.
64 S. E. Wolf, L. Muller, R. Barrea, C. J. Kampf, J. Leiterer, U. Panne, T. Hoffmann, F. Emmerling and W. Tremel, *Nanoscale*, 2011, **3**, 1158–1165.
65 M. Balz, H. A. Therese, J. Li, J. S. Gutmann, M. Kappl, L. Nasdala, W. Hofmeister, H. J. Butt and W. Tremel, *Adv. Funct. Mater.*, 2005, **15**, 683–688.
66 J. Zhu, L. Huang, M. Cui and L. Ma, *CrystEngComm*, 2015, **17**, 1010–1014.
67 G. D. Rees, R. Evans-Gowing, S. J. Hammond and B. H. Robinson, *Langmuir*, 1999, **15**, 1993–2002.
68 J. W. Xiao and S. H. Yang, *CrystEngComm*, 2010, **12**, 3296–3304.
69 E. Loste, R. J. Park, J. Warren and F. C. Meldrum, *Adv. Funct. Mater.*, 2004, **14**, 1211–1220.
70 A.-W. Xu, W.-F. Dong, M. Antonietti and H. Cölfen, *Adv. Funct. Mater.*, 2008, **18**, 1307–1313.

